Correspondence to:
L. Shihora,
linus.shihora@gfz-potsdam.de

Non-Tidal Background Modeling for Satellite Gravimetry Based on Operational ECWMF and ERA5 Reanalysis Data: AOD1B RL07

Linus Shihora[1] [iD]**, Kyriakos Balidakis[1]** [iD]**, Robert Dill[1]** [iD]**, Christoph Dahle[1]**, **Khosro Ghobadi-Far[2]** [iD]**, Jennifer Bonin[3]** [iD]**, and Henryk Dobslaw[1]** [iD]

[1]GFZ German Research Centre for Geosciences, Potsdam, Germany, [2]Department of Geosciences, Virginia Tech, Blacksburg, VA, USA, [3]University of South Florida, St. Petersburg, FL, USA

Abstract The Atmosphere and Ocean De-Aliasing Level-1B (AOD1B) product provides a priori information about temporal variations in the Earth's gravity field induced by non-tidal circulation processes in atmosphere and ocean. It is routinely applied as a background model in the Gravity Recovery and Climate Experiment (GRACE)/GRACE Follow-On (GRACE-FO) satellite gravimetry data processing. We here present three new datasets in preparation for the upcoming release RL07 of AOD1B, that are based on either the global ERA5 reanalysis or the ECMWF operational data together with simulations from the Max-Planck-Institute for Meteorology general circulation model forced consistently with the fields of the same atmospheric data set. The oceanic simulations newly include an updated bathymetry around Antarctica including cavities under the ice shelves, the explicit implementation of the feedback effects of self-attraction and loading to ocean dynamics as well as a refined harmonic tidal analysis. Comparison to the current release of AOD1B in terms of GRACE-FO K-band range-acceleration pre-fit residuals, LRI line-of-sight gravity differences and band-pass filtered altimetry data reveals an overall improvement in the representation of the high-frequency mass variability. Potential benefits of enhancing the temporal resolution remain inconclusive so that the upcoming release 07 will be sampled again every 3 hr.

Plain Language Summary Satellite gravimetry missions such as the Gravity Recovery and Climate Experiment (GRACE) and GRACE Follow-On (GRACE-FO), which play a vital role in the monitoring of the Earth's mass transports, require a priori background information on the high-frequency mass variations which can not be resolved by the monthly gravity solutions. The Atmosphere and Ocean De-Aliasing Level-1B (AOD1B) data product provides the required background information for non-tidal high-frequency mass changes in the atmosphere and oceans. However, the accurate representation of these mass variations remains challenging and deficiencies in the background models have a significant impact on the overall gravity field errors. Thus, we here present three new datasets in preparation for an upcoming release of AOD1B (RL07). The datasets improve over previous releases by incorporating the effects of the self attraction and solid earth deformation caused by anomalous water masses (SAL), an improved representation of the bathymetry and atmospheric forcing around Antarctica, making use of the new ERA5 atmospheric reanalysis as well as an updated estimation and subtraction of atmospherically induced tidal signals. We compare the new data to the previous release of AOD1B using microwave- and laser-ranging data from GRACE-FO as well as Jason-3 altimetry data and show a global improvement in the representation of high-frequency mass changes.

1. Introduction

For nearly 20 years, the Gravity Recovery and Climate Experiment (GRACE; Tapley et al., 2004) and its successor mission GRACE Follow-On (GRACE-FO; Landerer et al., 2020) have provided global gravity fields monitoring large-scale mass re-distributions. These measurements have found a wide array of applications such as in monitoring terrestrial water storage and droughts (Boergens et al., 2020) or estimating the mass loss of the Greenland ice sheet (Sasgen et al., 2020). Bottom pressure anomalies estimated from GRACE data have also been used to infer changes in the North Atlantic Overturning Circulation (Landerer et al., 2015). As such, GRACE and GRACE-FO have made vital contributions to our understanding of environmental changes on our planet (Rodell et al., 2018; Tapley et al., 2019).

There are, however, challenges in the gravity retrieval that are inherent to the measurement principle of satellite gravimetry. Due to the polar orbit with a revolution period of about 90 min, satellite data is usually accumulated for a certain period of time (typically 30 days) for the computation of a global gravity field. Mass changes on time-scales shorter than twice the accumulation period (i.e., two months) cannot be resolved and cause what is known as temporal aliasing artifacts. To avoid such adverse effects, the GRACE Atmosphere and Ocean De-Aliasing Level-1B (AOD1B) product provides a priori background information on high-frequency mass variations in the atmosphere and the oceans based on scientific knowledge that is independent of the satellite gravity data. Provided by Deutsches GeoforschungsZentrum (GFZ), the sixth release of AOD1B (RL06, Dobslaw et al., 2017) is applied by all of the major GRACE/GRACE-FO processing centers worldwide.

Background models are inevitably imperfect in capturing high-frequency variability. Errors are substantially higher in the oceanic component in view of the poorly developed ocean observing system for rapid wind-driven flow compared to atmospheric reanalyses. This is especially true for purely atmospherically forced oceanic simulations without constraints from observations. Full-scale simulations of the GRACE-FO mission (Flechtner et al., 2016) indicate that errors in the non-tidal background models, along with accelerometer noise and ocean tide model deficits, form a major contribution to the overall GRACE-FO gravity field errors. In fact, recent assessments of experimental daily GRACE solutions (Schindelegger et al., 2021) and band-pass filtered satellite altimetry data (Bonin & Save, 2020) clearly indicate both regions and time-scales for further improvements of in particular the oceanic part of AOD1B.

In this study we introduce three experimental datasets (v72, v73, and v74) in preparation of the next release RL07 of AOD1B. In Section 2 we provide details on the datasets in terms of the atmospheric surface pressure, upper air contributions, simulated ocean bottom pressure and transformation into Stokes coefficients. Subsequently, we assess whether ECMWF model changes have an impact on the temporal consistency of the data in Section 3, and address the impact of possibly higher temporal resolution in Section 4. The datasets are then compared to the current release RL06 in terms of GRACE-FO K-band range-acceleration (KBRA) pre-fit residuals (Section 6), line-of-sight gravity differences as measured by the GRACE-FO Laser Ranging Instrument (Section 7), and band-pass filtered altimetry data (Section 8), before we conclude with a final assessment and summary in Section 9.

2. Characteristics of AOD1B RL07

AOD1B RL07 will consist of an atmospheric component based on ECMWF operational and reanalysis data, and an oceanic component based on unconstrained simulations with the Max-Planck-Institute for Meteorology Ocean Model (MPIOM) which is consistently forced with the fields from the corresponding atmospheric model. All three experimental datasets presented here were calculated for the year 2019. Two solutions are based on atmospheric data from ECMWF's ERA5 reanalysis (Hersbach et al., 2020) and given either at hourly (v72) or 3-hourly (v73) time-steps. The data set v74 is based on ECMWF's operational numerical weather prediction (NWP) model and is given at 3-hourly time-steps. For each experiment, the atmospheric data set is also used as forcing of the corresponding oceanic simulation by making use of the hourly temporal sampling where available.

2.1. Atmospheric Surface Pressure

Air pressure variations at the surface largely dominate the high-frequency gravity variations induced by atmospheric processes above the continents. Surface pressure is generally decreasing with height, and its representation in models thus critically depends on the height of the surface orography, which varies substantially between individual model configurations. To ensure consistency of the surface pressure time-series, we reduce all datasets to a common reference orography (Dobslaw, 2016) in the same way as for AOD1B RL06.

As AOD1B aims to only describe non-tidal mass variability signals, high-frequency tidal signatures must be estimated and removed from the data set. Atmospheric tides are primarily induced through the absorption of infrared and ultraviolet radiation in the middle atmosphere as well as periodic deformations of the Earth's crust and sea surface (Dieminger et al., 1996). These signals are removed from the atmospheric data through a harmonic analysis. We consider in total 16 tidal constituents in the least-squares adjustment as given in Table 1, based on the years 2007–2014. The choice of frequencies is based on several criteria such as (a) a minimal amplitude of 10 Pa locally, and (b) a certain spatial coherence of the waves with similar phases over distances of several hundred km.

Table 1

Partial Tidal Waves Reduced From AOD1B RL07 and the Associated Astronomical Arguments as a Function of the Mean Solar Time at Greenwich t, the Mean Longitude of the Moon s, the Mean Longitude of the Sun h, and the Longitude of the Sun's Mean Perigee p_s

Darwin name	Frequency (°h⁻¹)	Astronomical argument
$\pi1$	14.91786609	$t - 2h + p_s - 90°$
P1	14.95893277	$t - h - 90°$
S1	15.00000141	$t + p_s + 90°$
K1	15.04107005	$t + h + 90°$
$\psi1$	15.08213673	$t + 2h + p_s + 90°$
M2	28.98410705	$2t - 2s + 2h$
T2	29.95893614	$2t - h + p_s$
S2	30.00000282	$2t - 90°$
R2	30.04106950	$2t + h - p_s + 180°$
K2	30.08214010	$2t + 2h$
T3	44.95893559	$3t - h$
S3	45.00000423	$3t + 180°$
R3	45.04107287	$3t + h$
S4	60.00000564	$4t$
S5	75.00000705	$5t$
S6	90.00000846	$6t$

Note. The mean solar time τ is given by $\tau = t - s + h$.

In contrast to AOD1B RL06 the harmonic analysis newly includes the $\pi1$, $\psi1$, K2, S4, S5, and S6 constituents while not considering N2 and L2, which turned out to be negligible in the most recent atmospheric reanalysis ERA5.

Initially, we focus on the comparison of surface pressure from ERA5 and the ECWMF operational data both given at 3 hourly intervals after mapping to a common reference orography and subtraction of atmospheric tides (Figure 1a). Standard deviations of differences calculated for the year 2019 are well below 80 Pa globally, while most of the signal is found along the Antarctic circumpolar current (ACC) where in-situ data coverage is sparse and storm events are imminent. We note that those differences are small with respect to differences with other state-of-the-art global atmospheric reanalyses, and can be related to the common code base of ECMWF's Integrated Forecast System (IFS) that is being used for both the ERA5 reanalysis and the operational NWP model. It is thus acceptable to concatenate ERA5 and the operational data at some point in time to make use of both the long-term consistency of the reanalysis and the low-latency availability of the operational data.

2.2. Upper Air Contributions

In addition to surface pressure, there is also a small contribution of upper-air density anomalies to the gravity field that should not be ignored for precise instruments as employed by GRACE and GRACE-FO (Swenson & Wahr, 2002).

The computation of the upper air density effects is based on a vertical integration of the atmospheric densities calculated at the original hybrid pressure-sigma (model) levels that are smoothly following the surface orography. Geopotential values at the 137 model levels are computed employing 3D temperature and specific humidity fields. After a transformation into mass increments, the gravitational effect is integrated vertically by summing up the contributions of each model level (Dobslaw et al., 2016). Subsequently, the gravitational effect of surface is subtracted to only retain the effects of the upper-air masses. Note that no reference orography is employed here but all calculations refer to the original model orography and the associated vertical discretization. We refer the interested reader to Dobslaw et al. (2016) for further details.

Upper-air anomalies were calculated from 3-hourly ERA5 and operational ECMWF data for the whole year 2019. To facilitate comparison, gravity potential differences are synthesized back into the spatial domain and are displayed in terms of corresponding surface pressure anomalies. The standard deviations of the differences are displayed in Figure 1b. The signals are one order of magnitude smaller than the remaining differences of surface
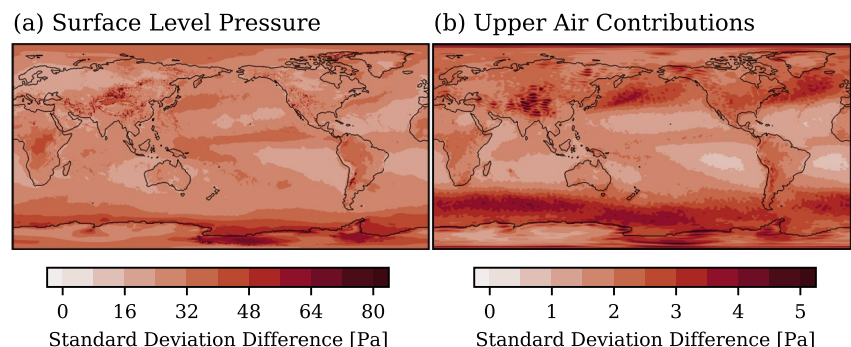

(a) Surface Level Pressure   (b) Upper Air Contributions

0 16 32 48 64 80
Standard Deviation Difference [Pa]

0 1 2 3 4 5
Standard Deviation Difference [Pa]

Figure 1. Standard deviation of differences between ERA5 and ECMWF operational surface level pressure (a) and upper air contributions (b). ERA5 data is sub-sampled to 3 hourly epochs to ensure equal temporal sampling of both datasets.
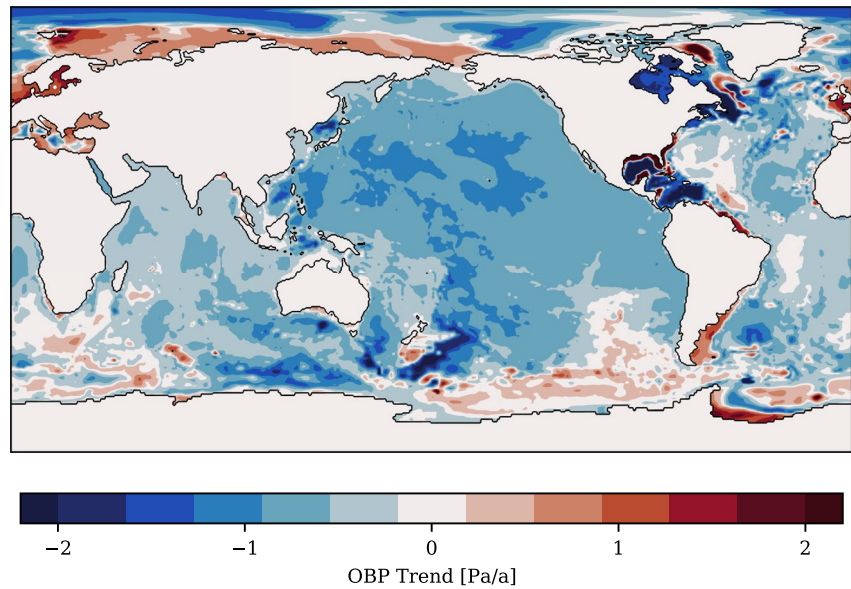
Figure 2. Linear trend in ocean bottom pressure over the last 50 years of the 2000 years long spin-up simulation.

anomalies and amount to 5 Pa only. The largest signals are found in regions of the mid-latitude storm tracks which roughly corresponds to the band of the ACC at the southern hemisphere.

2.3. Ocean Bottom Pressure

To complement the atmospheric mass variability, AOD1B uses simulations based on MPIOM (Jungclaus et al., 2013). MPIOM is a free surface general circulation model that solves the primitive equations under the Boussinesq approximation (Marsland et al., 2003). Here, we make use of MPIOM's TP10L40 configuration which uses a 1.0° tri-polar Arakawa-C grid with 40 vertical layers and nominal internal model time-step of 20 min. The model contains a dedicated sea-ice module. Most recently, the full feedback of self-attraction and loading has been implemented (Shihora, Sulzbach, et al., 2022) and the spatial domain has been extended to also include cavities underneath the Antarctic shelf-ice.

Model experiments were initialized from climatologies of observed 3D ocean temperature and salinity distributions (Levitus et al., 2005) followed by a 2000 years long spin-up run under cyclic atmospheric forcing with daily sampling (Röske, 2005).

Residual linear trends in ocean bottom pressure (OBP) during the last 50 years of the spin-up simulation are well below 2 Pa/a on regional scales and below 4 Pa/a for all individual grid points (Figure 2). The largest trends are found in (semi-) enclosed seas, which typically take longer to reach a state of equilibrium due the limited exchange of water masses with the open ocean. We note, however, that further spin-up would hardly reduce those residual trends significantly, since these signals are, in fact, not linear, but overlaid by substantial decadal-to-centennial ocean variability. In view of the small magnitude of the remaining drift, we rate this state as fully acceptable starting point of all subsequent experiments with NWP forcing data.

By starting from the same initial state, a transient simulation with hourly ERA5 forcing data is integrated over the years 1980 until 2019. A second simulation with 3-hourly ECMWF operational forcing extending also until the end of 2019 is initiated in January 2018 with initial conditions taken from the ERA5 run. Note that the atmospheric forcing fields have been modified to accommodate the shielding effect of the shelf-ice by setting temperatures to −4° (Bernales et al., 2017), and wind stress as well as atmospheric freshwater fluxes to zero. Surface pressure forcing remains unaffected since it is propagated through the ice body. We also allow for the far-field attraction effects of atmospheric pressure variability on ocean dynamics as detailed in Shihora, Sulzbach, et al. (2022).
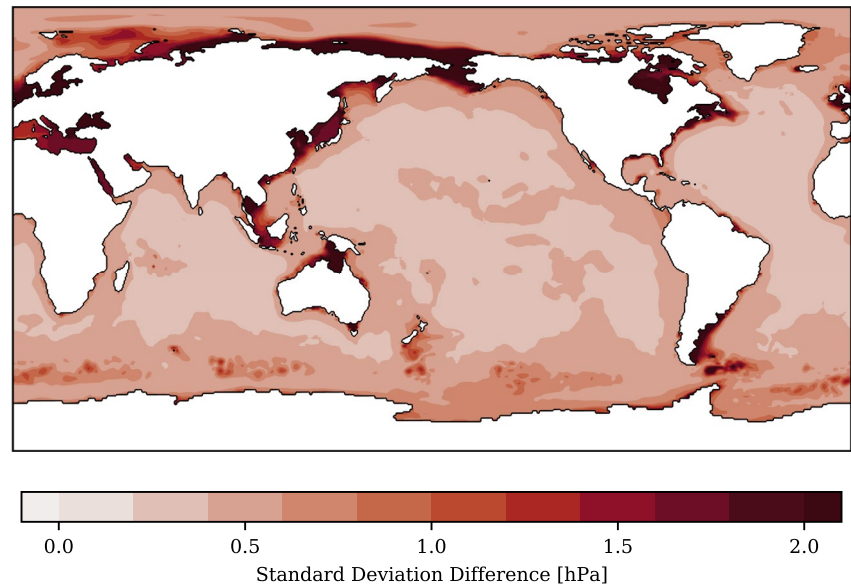
Figure 3. Standard deviation of difference in ocean bottom pressure between v73 and v74.

While both oceanic simulations do not explicitly include attraction from the luni-solar gravitational potential, tidal signals are still induced in the ocean simulation through periodic variations in atmospheric surface pressure and wind stress. The subtraction is done using the same procedure as described above for the atmosphere. Again, 16 tidal constituents are considered and the estimation is performed for a single year 2019 only. Please note that this estimation is performed independently for both ocean model experiments.

Additionally, we account for artificial fluctuations in the total ocean mass induced by the Boussinesq approximation included in MPIOM's prognostic equations by subtracting the mean bottom pressure signal averaged over the entire ocean domain (Greatbatch, 1994).

In the following, hourly data from the ERA5 experiment is labeled as v72. Data from the same experiment that is sub-sampled to 3 hr by selecting every third time-step will be referred to as v73. The 3-hourly data from the simulation with operational forcing is called v74 in the reminder of this paper.

As a first step, we are assessing the impact of different atmospheric forcing sources on the simulated ocean bottom pressure by looking at the standard deviation of the differences between v73 and v74 each after subtracting the estimated tidal signals (Figure 3). In most of the open ocean the differences are well below 0.5 hPa, with a spatial average over the entire ocean domain of 0.55 hPa. A slightly increased difference in variability is found in the southern ocean in the region of the ACC which is the region with the largest variability driven by the atmospheric forcing. We find also strong signals of up to 2 hPa in several coastal and shelf regions. In these regions, most of the variability is in the sub-daily frequency band and thus differences in the spatial and temporal resolution of the atmospheric forcing have a correspondingly stronger impact.

Additionally, we also assess the differences between v74 and the oceanic simulation of AOD1B RL06, which is also forced with ECMWF's operational data in the year 2019 (Figure 4). The simulated OBP is very similar in the tropical and subtropical open ocean with a global average of the standard deviation difference of just under 1 hPa. Notable discrepancies are found in coastal regions and enclosed seas such as the Gulf of Carpentaria, where the effects of SAL have a significant impact (Ghobadi-Far et al., 2022). The most significant differences, however, are found in the southern ocean in the region of the ACC. Here, model changes in MPIOM between v74 and RL06 such as the feedback from SAL as well as the inclusion of cavities under the Antarctic ice-shelves have a rather strong effect (Schindelegger et al., 2021; Shihora, Sulzbach, et al., 2022).
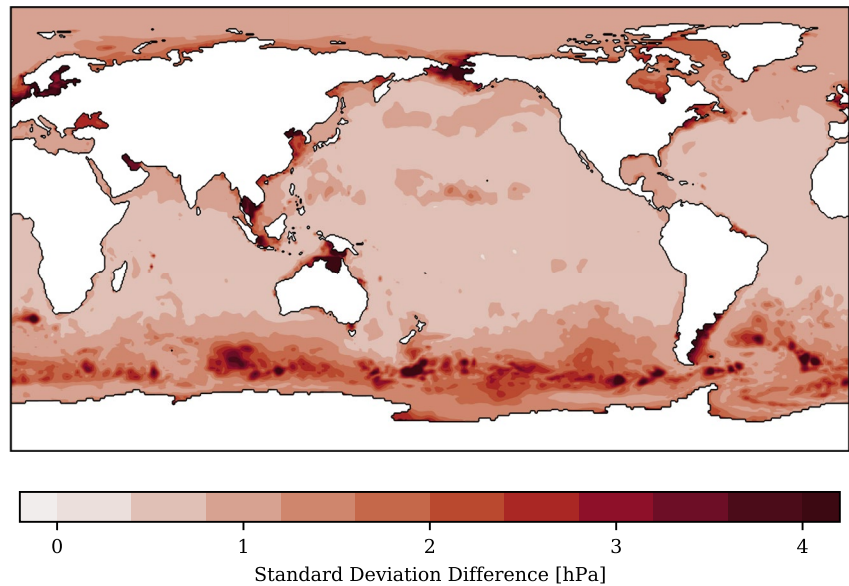
Figure 4. Standard deviation of difference in ocean bottom pressure between v74 and AOD1B RL06.

2.4. Transformation Into Stokes Coefficients

Time variable background models are traditionally provided in terms of Stokes coefficients. As for previous releases, RL07 will be made available up to spherical harmonic degree and order 180. Four individual sets of coefficients (i.e., ATM, OCN, GLO, and OBA) will be provided at each time-step that contain individual signal components of the coupled atmosphere-ocean system.

The ATM coefficients contain the contribution of atmospheric surface pressure over the continents, the static contribution of atmospheric surface pressure to OBP elsewhere, and the contribution of upper-air density anomalies over both the continents and ocean. OCN contains the contribution of the dynamic ocean to OBP while excluding the static contribution of the atmosphere. The GLO coefficients form the combination of the ATM and OCN coefficients and are usually applied in precise orbit determination. Finally, OBA are set to zero over the continents and contain the simulated OBP including the surface pressure contribution over the oceans. OBA coefficients deviate from the GLO coefficients by disregarding the comparatively minor contribution of the upper air density anomalies. A detailed description of the data-products including file formats is given in Dobslaw et al. (2016).

In contrast to previous AOD1B datasets we here also make use of an ellipsoidal reference surface during the transformation of the OBP fields into Stokes coefficients (Dobslaw et al., 2016) which so far has been used only for the atmospheric components (Ghobadi-Far et al., 2019; Petit & Luzum, 2010). To demonstrate the potential impact, Stokes coefficients were computed both at a spherical (as in RL06) and an ellipsoidal surface. After back-transformation into the spatial domain, standard deviations of the differences are shown in Figure 5. Signal magnitudes of up to 2 hPa underline the importance of applying a proper reference surface. Please note that most of the ocean bottom pressure variability is also associated with a corresponding sea-level change induced by changes in wind forcing. It is therefore reasonable to assume that most of the mass change happens close to mean sea-level (which is well approximated by an ellipsoidal surface) and not at the ocean sea floor.

3. Impact of ECMWF Model Changes

It is important to recall that ECMWF operational data is supplied regularly for many years already, and modern improvements to the forecast system are implemented through occasional updates of the Integrated Forecasting System (IFS). Data set v74, as it is based on the operational data for the year 2019, includes the transition to the IFS cycle 46R1 on June 11th, which implements changes in the data assimilation, observation handling, and
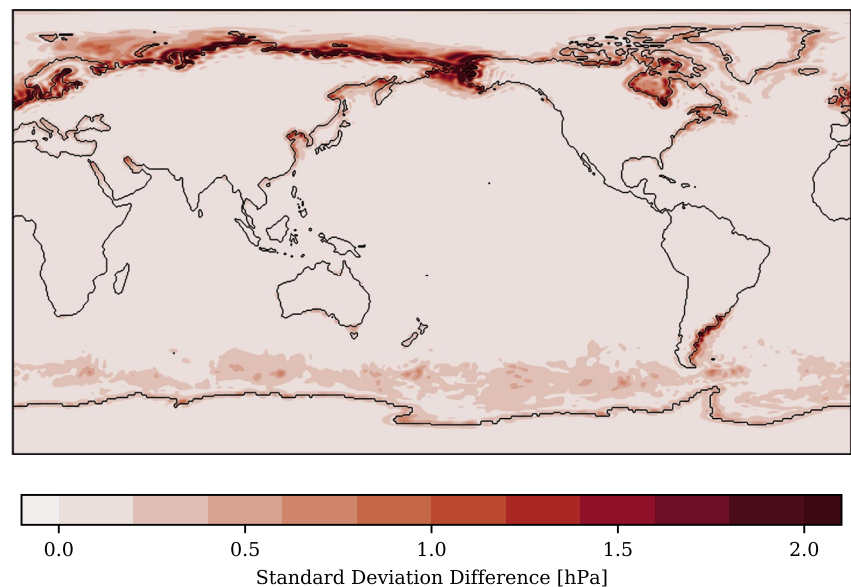
Figure 5. Influence of the change to an ellipsoidal reference surface. Differences in the OCN coefficients of v74 when using either a spherical or ellipsoidal reference surface are transformed back to a grid and shown in terms of the standard deviation.

physical model changes. We thus assess if and to what degree the transition in the IFS affects the data set v74 as an example of such regular IFS upgrades that typically take place once or twice per year.
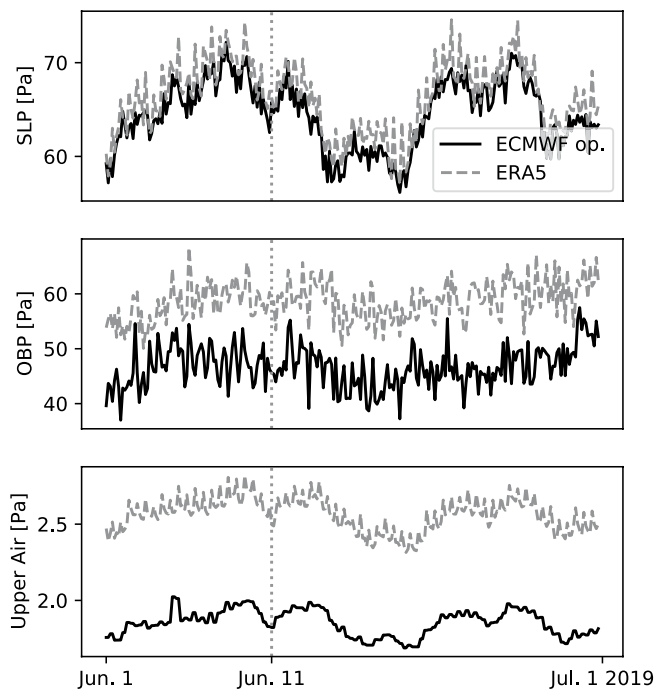

Figure 6. Spatially averaged absolute value of 3 hourly tendencies for June 2019 which includes the change to the Integrated Forecasting System cycle 46R1 of the ECMWF operational forecasts. Tendencies are given for atmospheric surface level pressure, simulated ocean bottom pressure, and upper-air anomalies. Black indicates ECMWF operational based data used in v74, while gray represents ERA5 based data as used in v73.

We therefore calculate the spatially averaged absolute values of the 3 hourly tendencies, which are computed as differences between consecutive 3 hourly time-steps, for the month of June 2019 around the time of the model change (11 June). Tendencies are shown for the atmospheric surface pressure (top), simulated bottom pressure (middle) and upper air contributions (bottom). Black curves here represent the ECMWF operational based data, while gray represents the ERA5 based data set of v73. To recall, the key feature of atmospheric reanalyzes is the application of the same model configuration for the whole analysis period. v73 thus serves as a reference that is not affected by any such changes in the IFS. Any prominent offset in a simulated quantity would manifest as a prominent spike in the tendencies.

Figure 6 confirms no significant impact of the IFS model change in 2019 on quantities relevant for satellite gravimetry. The temporal variations of the tendencies are very comparable between v73 and v74 and can be explained by the prevailing weather situation during those days. We note a slightly higher level (20%) of the tendencies from ERA5 for both OBP and the upper air contributions, which might be due to a slightly different handling of the wind stress and the different spatial resolutions of both atmospheric models. At the date of the IFS transition, no increase in tendencies is found, so that there are thus no indications for any adverse influence of the IFS cycle 46R1 model change on quantities relevant for the calculation of AOD1B.

4. Impact of Tidal Reduction

As noted above, tidal waves are estimated and removed from the non-tidal variability that remains in AOD1B. To assess the impact of this separation, we show the resulting reduction in sub-daily variability for the ERA5 surface pressure, upper-air contributions and OBP (Figure 7) before (left) or after (right) the harmonic analysis.
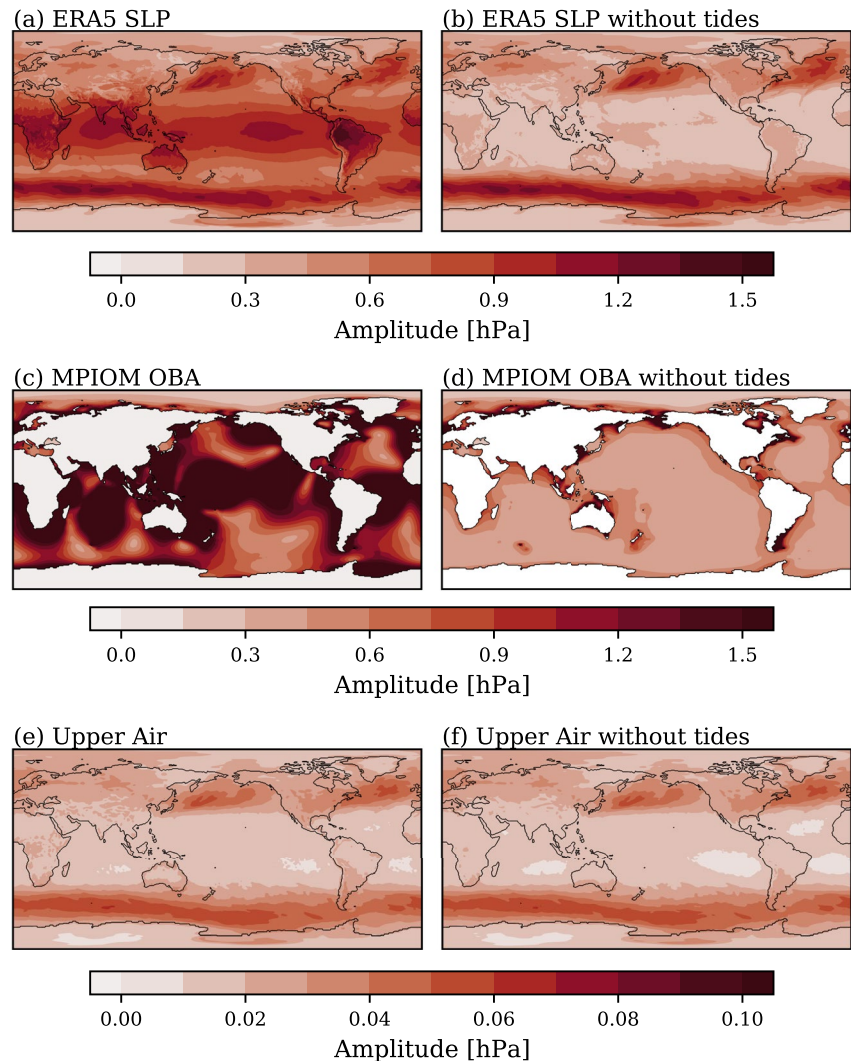
Figure 7. Sub-daily variability of ERA5 surface pressure (a, b), Max-Planck-Institute for Meteorology Ocean Model ocean bottom pressure (c, d) and ERA5 based upper air anomalies (e, f) either including tidal signals (left) or after the removal of tidal signals (right).

For the surface pressure, atmospheric tides are very prominent at tropical latitudes, and the variability is reduced drastically at those latitudes, with a global average reduction of 47%. In the regions of mid-latitude storm tracks that are characterized by advecting cyclones, however, almost none of the sub-daily variability is explained by atmospheric tides. The picture is quite different for OBP, where hemispheric waves are excited by the periodic atmospheric forcing leading to the establishment of distinct large-scale amphidromic systems with strong variability in particular along the coasts of major ocean basins. For OBP the reduction in variability is even stronger than for the surface pressure with a global average of 57%. For the upper-air contributions, on the other hand, the impact of atmospheric tides is very minor and can be, in fact, safely neglected in the processing of AOD1B.

5. Impact of Temporal Resolution

RL06 of AOD1B and the datasets v73 and v74 are all given with 3 hourly resolution. Since the ERA5 reanalysis is even available with hourly resolution, it is important to assess the possible gain of such an enhanced temporal resolution. To do so, we sub-sample the hourly v72 data to three hourly fields and interpolate back linearly to an hourly sampling in the same way as it would have been made in GRACE precise orbit determination to arrive at
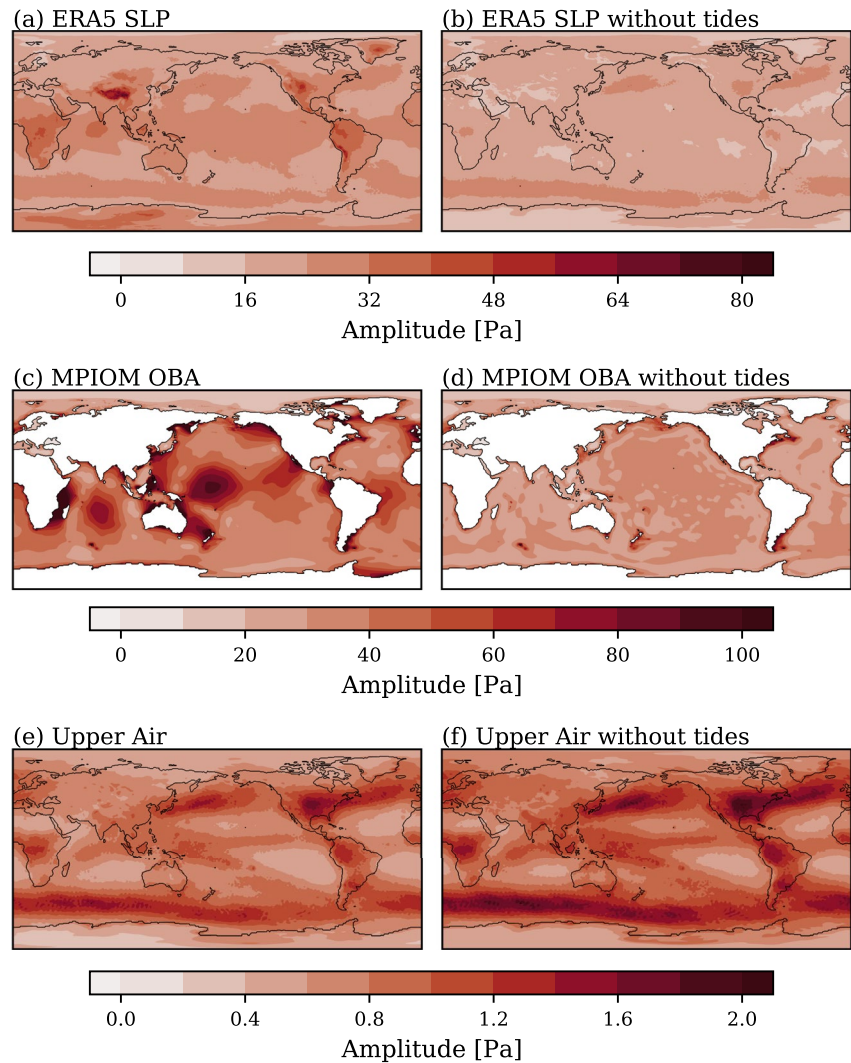
Figure 8. Standard deviation of differences between original hourly data and three-hourly data linearly interpolated to hourly epochs for ERA5 surface pressure (a, b), Max-Planck-Institute for Meteorology Ocean Model ocean bottom pressure (c, d) and ERA5 based upper air anomalies (e, f). Figures are given either containing tidal signals (left) or after the subtraction of tidal signals (right).

background model values for arbitrary epochs in time. Subsequently, the standard deviation of the differences is computed between the original and interpolated data.

Standard deviations of differences for surface pressure, OBP and the upper air contributions show negligible benefits of the hourly temporal resolution particularly after the removal of the tidal signals (Figure 8). We thus conclude that three hourly data can easily be interpolated to higher temporal resolutions without greatly compromising the high-frequency variability. The influence of linear interpolation to hourly values only introduces differences of up to 0.5 hPa provided that tidal signals are carefully removed from the underlying data set. AOD1B RL07 will be therefore provided again with a 3-hourly sampling.

6. Impact on GRACE-FO K-Band Pre-Fit Residuals

We assess now the impact of the new background models on primary sensor data from the GRACE-FO mission. The analysis is based on KBRA pre-fit residuals obtained after data screening and precise orbit determination in the GFZ RL06 data processing (Dahle et al., 2019). The KBRA are computed by differentiating K-band range-rate residuals and applying a fifth order Butterworth filter with a cut-off frequency of 1/60 Hz. Subsequently, the
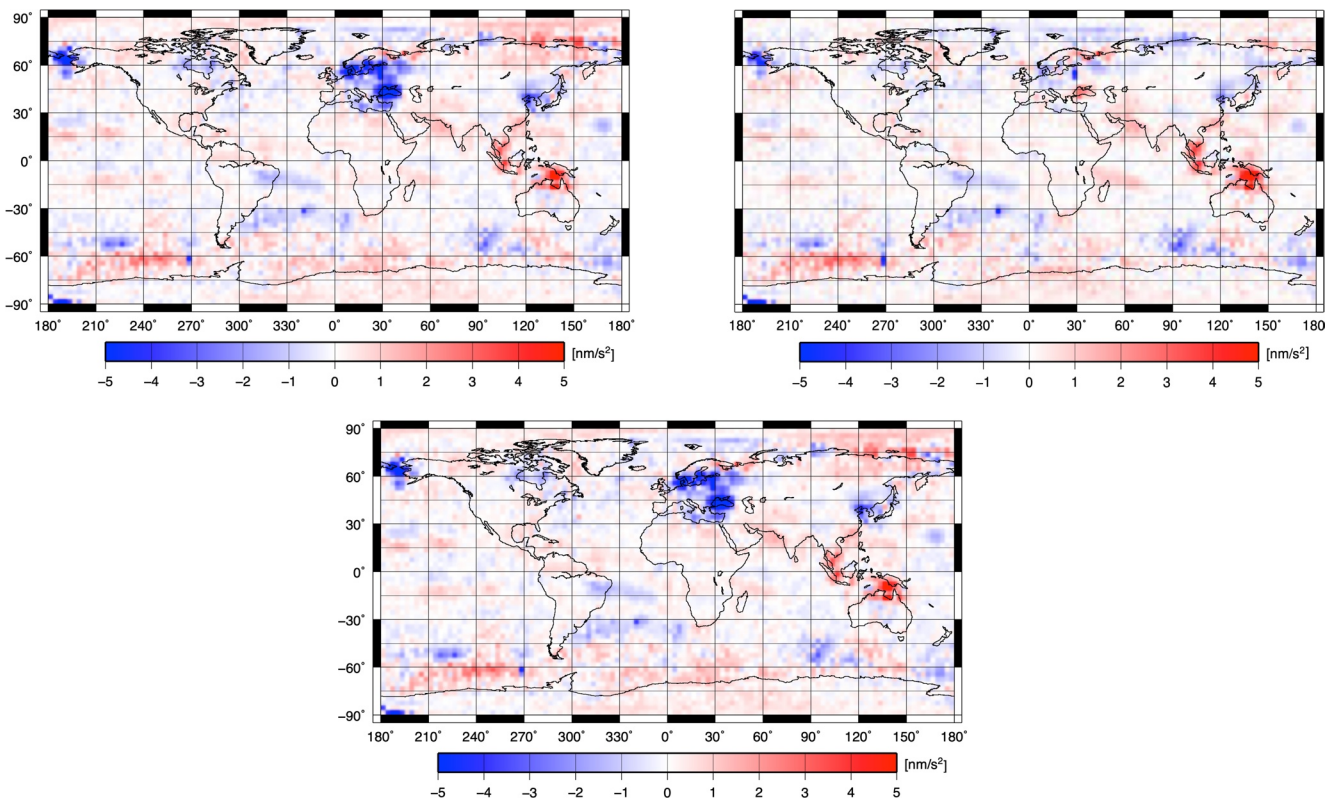
Figure 9. Difference of standard deviations of binned K-band range-acceleration pre-fit residuals for the entire year 2019. AOD1B RL06—v73 is given in the upper left, AOD1B RL06—v74 is given in the upper right. The lower subfigure shows the difference between v73 and v74. Positive values indicate an improvement, while negative values represent a degradation.

KBRA residuals are binned into cells with a 3° width before computing standard deviations for each of those grid cells.

Any improvement in the background model data would lead to a better fit with the measured satellite observations, that is, smaller observation residuals. Consequently, reductions in KBRA residual variability can be interpreted as improvements in the representation of the high-frequency variability in a test data set. The differences in standard deviation between KBRA residuals for the entire year 2019 are given in Figure 9 for comparisons between AOD1B RL06 and v73 (upper left), RL06 and v74 (upper right) as well as v73 and v74 (bottom).

Based on this assessment of real GRACE-FO data, we note improvements in several semi-enclosed regions as, for example, the Gulf of Carpentaria or the Gulf of Thailand, as well as improvements in the southern ocean in the region of the ACC, especially the Bellingshausen Basin. Slight degradations are visible for v73 in the region of the Black and Baltic Seas, which are related to a slight overestimation of the variability.

Additionally, we assess the area-weighted median of the KBRA pre-fit residual standard deviation differences between AOD1B RL06 and v74 for several regions in Table 2. We distinguish between deep and shallow oceanic regions (limit: $H = 1,000$m), tropics ($|\phi| = 23.5°$), northern latitudes ($23.5° < \phi < 66°$) and southern latitudes ($-23.5° < \phi < -66°$). The median is computed for all area-weighted grid points in each region requiring a minimal signal of 0.1 nm/s². Both on a global scale and the considered areas, v74 outperforms the current RL06 by at least 0.12 nm/s².

Table 2
Median of Differences in K-Band Range-Acceleration Pre-Fit Residuals Between AOD1B RL06 and v74 (Figure 9 Upper Right) for Different Regions

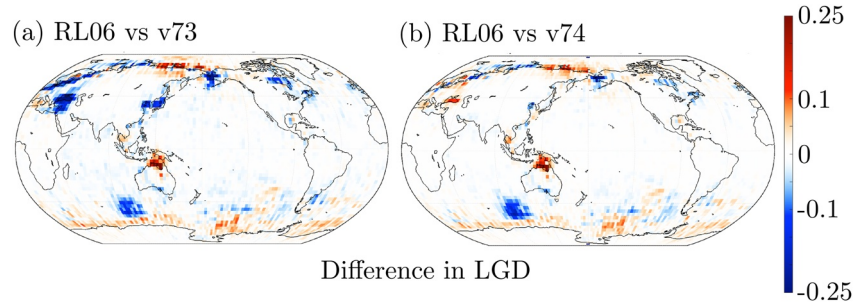| Region	Median of pre-fit differences (nm/s²)
Global	0.16
Shallow Waters	0.16
Deep Tropics	0.20
Deep Northern Lat.	0.16
Deep Southern Lat.	0.12

Figure 10. Differences in RMS variability of the laser ranging interferometer residuals in nm/s^2 between AOD1B RL06 and v73 (a) or v74 (b) for the year 2019. Positive values indicate an improvement, while negative values represent a degradation.

In summary, v73 and v74 are very comparable and show both regions of improvements compared to AOD1B RL06 that are quite consistent with results for the pair-wise model comparisons presented above.

7. Impact on GRACE-FO LRI Residuals

In addition to the KBR sensor, GRACE-FO is also equipped with a laser ranging interferometer (LRI) which measures the inter-satellite distance with higher precision (Abich et al., 2019). We use the LRI data in 2019 to study the impact of the new datasets. To that end, we first compute the LRI pre-fit residuals by removing the effect of static gravity and other well-known high-frequency geophysical signals like ocean tides from measured range-rate data. The range-acceleration residuals, obtained by numerical differentiation, are then used to compute the line-of-sight gravity difference (LGD) observations by applying a transfer function (Ghobadi-Far et al., 2020). By removing the slowly-varying time-variable gravity signals using the GRACE-FO Level-2 monthly solutions (Yuan, 2019), we obtain the sub-monthly (or post-fit) LGD LRI observations which partly reflect the high-frequency, non-tidal mass changes in the atmosphere and oceans. Note that, in contrast to KBR data, the improved accuracy of LRI residuals at higher frequencies by as much as one order of magnitude (Ghobadi-Far et al., 2020) allows for obtaining precise gravitational measurements without applying any low-pass filter.

The sub-monthly (post-fit) LRI residuals in terms of LGD are further reduced by gravitational signals computed from v73, v74 and AOD1B RL06. The difference in RMS variability of LRI residuals expressed in nm/s^2 (computed in 3° bins) with respect to these models is shown in Figure 10. Regions where the new test-data better matches the GRACE-FO LRI measurements are depicted in red, while areas of degradation are indicated in blue.

The results reveal general improvements in both cases in the southern ocean in the band of the ACC as well as the Gulf of Carpentaria and some regions along the Arctic coast. Additionally, v74 shows some improvements in the Mediterranean and Black Sea. There are, however, areas where the test data does not capture the variability as well as RL06 such as a region of the southern ocean to the south-west of Australia and the Bering-Sea. v73 also shows a slightly worse performance in some enclosed seas such as the Black and Baltic Seas or the Sea of Japan.

Table 3
Median of Differences in LRI Residuals Between AOD1B RL06 and v74 (Figure 10 Right) for Different Regions

Region	Median difference in RMS variability (nm/s^2)
Global	0.025
Shallow Waters	0.025
Deep Tropics	0.022
Deep Northern Lat.	0.021
Deep Southern Lat.	−0.020

We also compare RL06 and v74 in terms of global and regional median values as done in Section 6. The results are given in Table 3 and are computed for the same regions requiring a minimal signal of 0.02 nm/s^2. Considering the generally smaller magnitude of the LRI based values, the results in Table 3 are in most cases comparable to the ones given in the previous section, indicating a better performance of v74. Only in the deep ocean of the southern latitudes can the new data set not match the results from RL06 resulting in a negative median of −0.02 nm/s^2. On a global scale, however, v74 still captures the high-frequency variability better than RL06.

In general, the results clearly match the analysis based on KBRA pre-fit residuals, although the picture is more detailed thanks to the substantially lower noise level of the LRI.
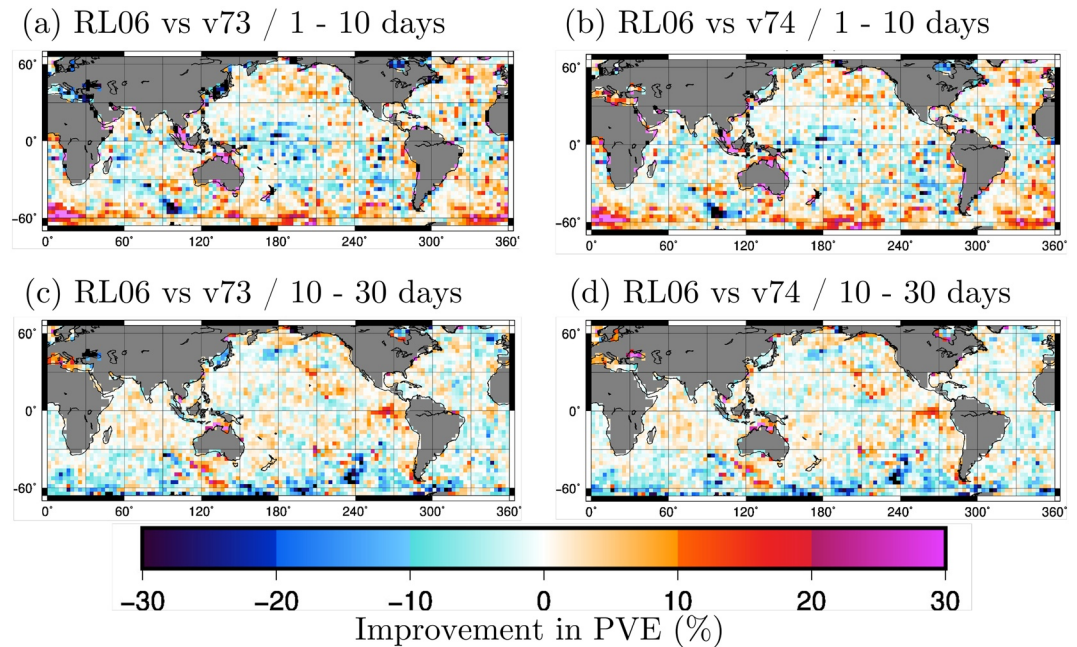
Figure 11. Differences in explained variance (PVE) between AOD1B RL06 and v73 (a, c) or v74 (b, d) using altimetry data as a base series.

8. Comparison Against Satellite Altimetry

To complete the assessment based on independent geodetic data, we also present a comparison with band-pass filtered along-track altimetry. Sea-level anomalies from the Jason satellites have previously been used to help to determine the accuracy of GRACE and underlying model data at sub-monthly timescales (Bonin & Chambers, 2011; Bonin & Save, 2021). While this method is not ideally suited for regions with a strong mesoscale activity or significant steric sea-level changes, it is still applicable for large parts of the open ocean especially when considered together with the GRACE-based analyses of the previous sections.

The comparison is performed by using Jason-3 along track data for the year 2019 with all standard corrections applied. The sea surface height signals are averaged daily before the application of a 300-km Gaussian filter to each global grid in order to reduce noise. This produces datasets comparable in spatial resolution to the AOD1B grids. For both altimetry and background models, the respective mean is subtracted and the data is binned into cells of 3° width. To extract the variability in a 10 days (20 or 30 days) frequency band a sliding window based on a Gaussian distribution with a full width at half maximum of 7 days (15 or 23 days) and a window length of 20 days (30 or 47 days) is applied. Finally, the percent of explained variance (PVE) is computed using the altimetry data as a base series as given in Equation 1,

$$PVE = \left(1 - \frac{\text{var}(Alt. - Model)}{\text{var}(Alt.)}\right) 100\%. \tag{1}$$

We show the differences in PVE between RL06 and v73/v74 using altimetry as a base series in Figure 11. In all cases red areas mark regions where the test-data better captures the variability observed by altimetry and vice-versa for the blue regions.

In the high-frequency band both test datasets show an improvement with respect to RL06 in regions of the southern ocean as well as some coastal areas such as the Gulf of Carpentaria or the Gulf of Thailand. For a region of the southern ocean south-west of Australia and some semi-enclosed seas however, RL06 still performs better. For the 10–30 days band there are still some improvements to be found in coastal areas but a reduced performance in the southern ocean.

Table 4
Change in Percent of Altimetry's Variance Explained by AOD1B RL06 Compared to v74 for Different Regions

Region	Change in PVE (%)		
	P < 10 days	10 < P < 30 days	P < 30 days
Global	0.67	−0.45	0.55
Shallow Waters	5.84	2.82	4.46
Deep Tropics	−1.38	0.15	−0.09
Deep Northern Lat.	1.29	−0.07	0.91
Deep Southern Lat.	1.43	−2.18	0.20

Note. Results are split into three frequency bands.

In line with the two previous sections, we here also quantify the difference between v74 and RL06 by computing the change in PVE globally as well as for the oceanic regions described in Section 6. In order to give more detail on the temporal behavior of the analysis, we split the results into three frequency bands. Results in Table 4 are given for frequencies below 10 days, between 10 and 30 days as well as all frequencies below 30 days. In general, the results match our findings in previous sections. Improvements are clearly visible on a global scale and especially in shallow regions. Mixed results are found for the tropics which can be linked to the generally low signal in the region especially in an analysis based on relative values. A reduction in performance is found in the low-frequency band in the southern ocean. Here RL06 clearly performs better than v74. The results are, however, compensated by a better performance in the high-frequency band resulting still in an overall improvement.

9. Summary and Conclusions

In this study, we have assessed three new background model datasets in preparation of the next release RL07 of the GRACE Atmosphere and AOD1B product. The datasets v72 and v73 consist of an ERA5-based atmospheric component while v74 is based on ECMWF operational data. The oceanic component of all three datasets derives from simulations with the MPIOM general ocean circulation model which newly includes cavities underneath the Antarctic ice-shelf as well as the full feedback from the effects of self-attraction and loading. In comparison to RL06, we also slightly revised the removal of relevant tidal signals and now utilize an ellipsoidal reference surface for the calculation of the Stokes coefficients. AOD1B RL07 is again provided as a spherical harmonic expansion complete up to degree and order 180 and in the same format as the previous versions.

An assessment of 3 hourly tendencies of the ECMWF operational based data shows that there is little indication of an impact of IFS model changes which are known to have impacted AOD1B in the past (Dobslaw et al., 2016). We also tested the possible gain of providing AOD1B with hourly resolution and found no significant improvements so that RL07 will retain the 3-hourly sampling introduced with RL06. The new background models have been also extensively tested with real geodetic data obtained by the satellites GRACE-FO and Jason-3. Results for K-band pre-fit residuals, LRI residuals, and band-pass filtered sea surface height anomalies are fairly consistent and document improvements with the new models. For the particular year 2019 assessed in this study, forcing data from the ECMWF operational model are slightly superior than the corresponding ERA5 data set. We thus decide to use ERA5 until December 2017 so that it covers the whole GRACE mission period, and will continue with operational data from January 2018 onwards which is well before the launch of GRACE-FO. ERA5-based coefficients will be also calculated internally for the years 2018 and 2019 to demonstrate the continuity across the transition period.

AOD1B RL07 is available at GFZs ISDC and published under Shihora, Balidakis, et al. (2022). Going forward, two further points will need to be addressed: (a) AOD1B is not only required to accurately represent the high-frequency mass variations but also needs to exhibit a temporal stability over long time-scales from years to decades to allow for a reliable signal separation of atmospheric mass change from the underlying terrestrial water cycle signals. This needs to be assessed both in terms of long-term trends as well as occasional jumps due to inevitable model changes. (b) The most recent assessment of model uncertainties for AOD1B was published for AOD1B RL05 only (Dobslaw et al., 2015), which is now believed to be too pessimistic in view of the latest improvements in background modeling. In view of the persisting dominance of oceanic errors in AOD1B, we plan to perform a series of ensemble runs with MPIOM under altered atmospheric forcing conditions to allow for the derivation of both a series of synthetic true errors to be used for simulations in line with Dobslaw et al. (2015) and also for the calculation of spatial error covariance matrices for the rigorous incorporation of stochastic information into the gravity field estimation process as recently developed by Abrykosov et al. (2021) for the case of ocean tides. We believe that such an update is particularly urgent in view of the ongoing specification process of a next generation gravity mission to be implemented jointly by ESA and NASA as a configuration of two GRACE-like satellite pairs that are operating at differently inclined orbits.

Data Availability Statement

The ERA5 reanalysis data is publicly available via the Climate Data Store at https://cds.climate.copernicus.eu (Hersbach et al., 2020). The GRACE-FO Level-1B and Level-2 data used in the LRI analysis are publicly available at https://podaac.jpl.nasa.gov/GRACE. Jason-3 GDR data is available via Lillibridge (2020). The GFZ GRACE-FO data as well as AOD1B RL06 can be accessed through GFZs Information System and Data Center under https://isdc.gfz-potsdam.de/. The final release of AOD1B RL07 is publicly available under the DOI https://doi.org/10.5880/GFZ.1.3.2022.003.

References

Abich, K., Abramovici, A., Amparan, B., Baatzsch, A., Okihiro, B. B., Barr, D. C., et al. (2019). In-orbit performance of the GRACE follow-on laser ranging interferometer. *Physical Review Letters*, *123*(3), 031101. https://doi.org/10.1103/PhysRevLett.123.031101

Abrykosov, P., Sulzbach, R., Pail, R., Dobslaw, H., & Thomas, M. (2021). Treatment of ocean tide background model errors in the context of GRACE/GRACE-FO data processing. *Geophysical Journal International*, *228*(3), 1850–1865. https://doi.org/10.1093/gji/ggab421

Bernales, J., Rogozhina, I., & Thomas, M. (2017). Melting and freezing under Antarctic ice shelves from a combination of ice-sheet modelling and observations. *Journal of Glaciology*, *63*(240), 731–744. https://doi.org/10.1017/jog.2017.42

Boergens, E., Güntner, A., Dobslaw, H., & Dahle, C. (2020). Quantifying the Central European Droughts in 2018 and 2019 with GRACE Follow-On. *Geophysical Research Letters*, *47*(14), 1672. https://doi.org/10.1029/2020GL087285

Bonin, J. A., & Chambers, D. P. (2011). Evaluation of high-frequency oceanographic signal in GRACE data: Implications for de-aliasing. *Geophysical Research Letters*, *38*(17), 1606. https://doi.org/10.1029/2011GL048881

Bonin, J. A., & Save, H. (2020). Evaluation of sub-monthly oceanographic signal in GRACE "daily" swath series using altimetry. *Ocean Science*, *16*(2), 423–434. https://doi.org/10.5194/os-16-423-2020

Bonin, J. A., & Save, H. (2021). Using GRACE to improve altimetry's ocean de-aliasing model. *Journal of Geophysical Research: Oceans*, *127*(1), e2021JC017711. https://doi.org/10.1029/2021JC017711

Dahle, C., Murböck, M., Flechtner, F., Dobslaw, H., Michalak, G., Neumayer, K. H., et al. (2019). The GFZ GRACE RL06 monthly gravity field time series: Processing details and quality assessment. *Remote Sensing*, *11*(18), 2116. https://doi.org/10.3390/rs11182116

Dieminger, W., Hartmann, G. K., & Leitinger, R. (1996). *Atmospheric tides* (pp. 97–109). Springer. https://doi.org/10.1007/978-3-642-78717-1_3

Dobslaw, H. (2016). Homogenizing surface pressure time-series from operational numerical weather prediction models for geodetic applications. *Journal of Geodetic Science*, *6*(1), 61–68. https://doi.org/10.1515/jogs-2016-0004

Dobslaw, H., Bergmann-Wolf, I., Dill, R., Poropat, L., & Flechtner, F. (2016). Product Description Document for AOD1B Release 06, Rev. 6.0. GFZ Potsdam, Potsdam, Germany. Retrieved from ftp://isdcftp.gfz-potsdam.de/grace/DOCUMENTS/Level-1/GRACE_AOD1B_Product_Description_Document_for_RL06.pdf

Dobslaw, H., Bergmann-Wolf, I., Dill, R., Poropat, L., Thomas, M., Dahle, C., et al. (2017). A new high-resolution model of non-tidal atmosphere and ocean mass variability for de-aliasing of satellite gravity observations: AOD1B RL06. *Geophysical Journal International*, *211*(1), 263–269. https://doi.org/10.1093/gji/ggx302

Dobslaw, H., Bergmann-Wolf, I., Forootan, E., Dahle, C., Mayer-Gürr, T., Kusche, J., & Flechtner, F. (2015). Modeling of present-day atmosphere and ocean non-tidal de-aliasing errors for future gravity mission simulations. *Journal of Geodesy*, *90*(5), 423–436. https://doi.org/10.1007/s00190-015-0884-3

Flechtner, F., Neumayer, K.-H., Dahle, C., Dobslaw, H., Fagiolini, E., Raimondo, J.-C., & Güntner, A. (2016). What can be expected from the GRACE-FO laser ranging interferometer for earth science applications? *Surveys in Geophysics*, *37*(2), 453–470. https://doi.org/10.1007/s10712-015-9338-y

Ghobadi-Far, K., Han, S.-C., McCullough, C. M., Wiese, D. N., Ray, R. D., Sauber, J., et al. (2022). Along-orbit analysis of GRACE follow-on inter-satellite laser ranging measurements for sub-monthly surface mass variations. *Journal of Geophysical Research: Solid Earth*, *127*(2), e2021JB022983. https://doi.org/10.1029/2021JB022983

Ghobadi-Far, K., Han, S.-C., McCullough, C. M., Wiese, D. N., Yuan, D.-N., Landerer, F. W., et al. (2020). GRACE follow-on laser ranging interferometer measurements uniquely distinguish short-wavelength gravitational perturbations. *Geophysical Research Letters*, *47*(16), e2020GL089445. https://doi.org/10.1029/2020GL089445

Ghobadi-Far, K., Šprlák, M., & Han, S.-C. (2019). Determination of ellipsoidal surface mass change from GRACE time-variable gravity data. *Geophysical Journal International*, *219*(1), 248–259. https://doi.org/10.1093/gji/ggz292

Greatbatch, R. J. (1994). A note on the representation of steric sea level in models that conserve volume rather than mass. *Journal of Geophysical Research*, *99*(C6), 12767–12771. https://doi.org/10.1029/94JC00847

Hersbach, H., Bell, B., Berrisford, P., Hirahara, S., Horányi, A., Muñoz-Sabater, J., et al. (2020). The ERA5 global reanalysis. *Quarterly Journal of the Royal Meteorological Society*, *146*(730), 1999–2049. https://doi.org/10.1002/qj.3803

Jungclaus, J. H., Fischer, N., Haak, H., Lohmann, K., Marotzke, J., Matei, D., et al. (2013). Characteristics of the ocean simulations in the Max Planck Institute Ocean Model (MPIOM) the ocean component of the MPI-Earth system model. *Journal of Advances in Modeling Earth Systems*, *5*(2), 422–446. https://doi.org/10.1002/jame.20023

Landerer, F. W., Flechtner, F. M., Save, H., Webb, F. H., Bandikova, T., Bertiger, W. I., et al. (2020). Extending the global mass change data record: GRACE follow-on instrument and science data performance. *Geophysical Research Letters*, *47*(12), e2020GL088306. https://doi.org/10.1029/2020GL088306

Landerer, F. W., Wiese, D. N., Bentel, K., Boening, C., & Watkins, M. M. (2015). North Atlantic meridional overturning circulation variations from GRACE ocean bottom pressure anomalies. *Geophysical Research Letters*, *42*(19), 8114–8121. https://doi.org/10.1002/2015GL065730

Levitus, S., Antonov, J., & Boyer, T. (2005). Warming of the world ocean, 1955–2003. *Geophysical Research Letters*, *32*(2), L02604. https://doi.org/10.1029/2004GL021592

Lillibridge, J. (2020). *Jason-3 Level-2 Operational, Interim and Final Geophysical Data Records (X-GDR), 2016 to Present (NCEI Accession 0122595). GDR. NOAA Office of Satellite Data Processing and Distribution*. NOAA National Centers for Environmental Information. Unpublished Dataset. Retrieved from https://accession.nodc.noaa.gov/0122595

Marsland, S., Haak, H., Jungclaus, J., Latif, M., & Röske, F. (2003). The Max-Planck-Institute global ocean/sea ice model with orthogonal curvilinear coordinates. *Ocean Modelling*, *5*(2), 91–127. https://doi.org/10.1016/S1463-5003(02)00015-X

Petit, G., & Luzum, B. (2010). IERS Convention (2010) (IERS Technical Note no. 36). Frankfurt am Main: Verlag des Bundesamtes für Kartographie und Geodäsie. Retrieved from http://www.iers.org/IERS/EN/Publications/TechnicalNotes/tn36.html

Rodell, M., Famiglietti, J. S., Wiese, D. N., Reager, J. T., Beaudoing, H. K., Landerer, F. W., & Lo, M.-H. (2018). Emerging trends in global freshwater availability. *Nature*, *557*(7707), 651–659. https://doi.org/10.1038/s41586-018-0123-1

Röske, F. (2005). Global oceanic heat and fresh water forcing datasets based on ERA-40 and ERA-15. *Reports on Earth System Science, 13*.

Sasgen, I., Wouters, B., Gardner, A. S., King, M. D., Tedesco, M., Landerer, F. W., et al. (2020). Return to rapid ice loss in Greenland and record loss in 2019 detected by the GRACE-FO satellites. *Communications Earth & Environment*, *1*(1), 8. https://doi.org/10.1038/s43247-020-0010-1

Schindelegger, M., Harker, A. A., Ponte, R. M., Dobslaw, H., & Salstein, D. A. (2021). Convergence of Daily GRACE solutions and models of submonthly ocean bottom pressure variability. *Journal of Geophysical Research: Oceans*, *126*(2), e2020JC017031. https://doi.org/10.1029/2020JC017031

Shihora, L., Balidakis, K., Dill, R., & Dobslaw, H. (2022). Atmosphere and Ocean Non-Tidal Dealiasing Level-1B (AOD1B) Product RL07. (GFZ Data Services). https://doi.org/10.5880/GFZ.1.3.2022.003

Shihora, L., Sulzbach, R., Dobslaw, H., & Thomas, M. (2022). Self-attraction and loading feedback on ocean dynamics in both shallow water equations and primitive equations. *Ocean Modelling*, *169*, 101914. https://doi.org/10.1016/j.ocemod.2021.101914

Swenson, S., & Wahr, J. (2002). Estimated effects of the vertical structure of atmospheric mass on the time-variable geoid. *Journal of Geophysical Research*, *107*(B9), ETG4-1–ETG4-11. https://doi.org/10.1029/2000JB000024

Tapley, B. D., Bettadpur, S., Watkins, M., & Reigber, C. (2004). The gravity recovery and climate experiment: Mission overview and early results. *Geophysical Research Letters*, *31*(9), L09607. https://doi.org/10.1029/2004GL019920

Tapley, B. D., Watkins, M. M., Flechtner, F., Reigber, C., Bettadpur, S., Rodell, M., et al. (2019). Contributions of GRACE to understanding climate change. *Nature Climate Change*, *9*(5), 358–369. https://doi.org/10.1038/s41558-019-0456-2

Yuan, D.-N. (2019). GRACE Follow-On JPL Level-2 Processing Standards Document. In *Jet Propulsion Laboratory, California Institute of Technology, California, USA. (For Level-2 Product Release 06)*.